

Research Paper

The relationship between atmospheric circulation, boundary layer and near-surface turbulence in severe fog-haze pollution periods

Zhengxuan Yuan^a, Jun Qin^{a,*}, Xiang Zheng^a, Yassin Mbululo^{a,b}

^a China University of Geosciences (Wuhan), School of Environmental Studies, Hubei, 430074, China

^b Department of Geography and Environmental Studies, Sokoine University of Agriculture, Tanzania



ARTICLE INFO

Keywords:

Pollution
Saddle pattern
Boundary-layer structure
Turbulence

ABSTRACT

Wind, temperature, relative humidity and aerosol mass concentration were monitored simultaneously in Wuhan, China. Several observations were found after analyzing the physical fields of these data. It was obvious that weak pressure and saddle patterns occurred during fog-haze episodes. An inversion layer occurred before heavy fog-haze events and became thicker during fog-haze events. The boundary layer structure index was relatively higher during fog-haze days and had a significant negative correlation with the planetary boundary layer height and turbulence parameters. Wind speeds were generally less than 5 m/s and rarely exceeded this speed on the selected polluted days. Turbulence variation characteristics had special representations, especially before fog-haze events. Turbulence intensities always reached abnormal peak values before fog-haze processes, while the intensities remained steady before and during pollution processes with low relative humidity. Both the turbulence kinetic energy and momentum flux decreased to near zero before heavy fog-haze processes. Momentum flux often presented abnormal disturbances before heavy fog-haze processes. These disturbances were often in an active phase before and during pollution processes with low relative humidity, a situation that is not similar to fog-haze events that maintained high relative humidity. There was a feedback mechanism between solar radiation and aerosol mass concentration, and the occurrence of turbulence anomalies may be related to the regulation of atmospheric circulation by wave-flow interaction. The results presented in this study suggest that the turbulence parameters, which display anomalies before the occurrence of heavy fog-haze processes under the background of inversion layers and stable atmospheric patterns, can serve as a means of predicting disastrous weather conditions such as fog-haze pollution.

1. Introduction

Air pollution problems have become an area of concern for most people, especially in China. Wuhan city experiences serious aerosol pollution during wintertime and ozone pollution during summertime. These air pollutants have serious negative impacts on people's health and the environment. As a result, observation and analysis of air pollution have received significant attention from a number of experts in the field of meteorology and air quality (Pasch et al., 2011; Wang et al., 2013; Petäjä et al., 2016; Philipp et al., 2016; Creamean et al., 2016). In addition, there have been numerous studies on the effects of climate on air quality, especially on summertime ozone air quality (Shen and Mickleby, 2017a, 2017b). These studies went further to the extent of developing a seasonal prediction model for summertime ozone.

It is worth noting that some studies on air pollution have focused

more on the analysis of surface layer observation data (Han et al., 2018; Zhong et al., 2017). Additionally, research by Li et al. (2017) pointed out that aerosol scattering and absorbing showed feedback to the diurnal evolution of the planetary boundary layer (PBL), which was crucial for understanding the interactions between air pollution and meteorology. A study by Zhong et al. (2017) showed the contribution of meteorological factors to an increase in pollutant concentration, but the governing mechanism was not well explained and almost nothing on the turbulence scale was considered. Likewise, studies on simulations (Miao et al., 2016; Gao et al., 2015; Bergot, 2013) focused on determining the feedback mechanism between aerosols and the boundary layer. Note that studies on turbulence characteristics have been conducted for many years (Wang et al., 2016; Ren et al., 2018). These studies mainly focused on analyzing the characteristics of turbulence parameters around special underlying surfaces during fog, fog-haze and dust events, but they

* Corresponding author.

E-mail address: qinjun@cug.edu.cn (J. Qin).

<https://doi.org/10.1016/j.jastp.2020.105216>

Received 16 May 2019; Received in revised form 14 December 2019; Accepted 2 February 2020

Available online 11 February 2020

1364-6826/© 2020 Elsevier Ltd. All rights reserved.

ignored abnormal turbulence signals. A recent study by Wei et al. (2018) on the intermittent turbulence contribution to the vertical diffusion of PM_{2.5} in North China pointed out that intermittent turbulent fluxes contributed positively to the vertical dispersion of PM_{2.5} and improved the air quality index (AQI) near the surface layer. This study introduced a possible mechanism for how intermittent turbulence affects the diffusion of PM_{2.5}, but unfortunately, it ignored turbulence anomalies before the onset of heavy pollution. Qin et al. (2018) found that the turbulence parameters in the near-surface layer appeared to be abnormal less than 130 min prior to heavy pollution events. To date, only a few studies have examined forecasting and warnings for heavy fog-haze events and extreme weather based on the characteristics of turbulence variations. Study by Wilcox et al. (2016) pointed out that reduced turbulence could exacerbate conditions favorable for low-visibility fog events. Studies by Wang et al. (2010), Wang et al. (2011) analyzed the turbulence parameters of the near-surface layer before and after storms and the weather conditions in the Huangshi area by using observation data collected from meteorological stations by three-dimensional ultrasonic anemometers. Their studies found that turbulent kinetic energy and intensity increased before heavy rainfall and snowstorms. Fluxes increased and reflected upward transport, and the turbulent fluxes before storms displayed an active phase. In addition, the turbulence kinetic energy and intensity had significant abnormal peak values. These findings differ from forecasts, which are often given by using common weather indicators; however, more case studies need to be examined. The mechanisms between such weather events and boundary-layer turbulence should also be given more attention.

Previous studies on turbulence variance characteristics have mainly focused on analysis of the turbulence parameters of the boundary layer during pollution processes or have considered only one kind of weather phenomenon. Thus, the following question arises: Is there any relationship among large-scale circulation, boundary layer structure and turbulence characteristics? Based on this question and the literature review presented above, this study applies the universality of our previous study (Qin et al., 2018). The relationship among large-scale circulations, boundary layer structure and turbulence characteristics throughout fog-haze events in the area surrounding Qingshan Bridge in Wuhan, China, will be established.

This paper is structured as follows. The data, study area and methods are described in Section 2. Section 3 analyzes the characteristics of the near-surface layer and shows the results. Section 4 provides conclusions and prospects. In this paper, local standard time (LST) is Beijing time (UTC + 8 h).

2. Methodology

2.1. Data sources

The ultrasound data used in this study were collected from an observation tower located at Qingshan Yangtze Bridge (114.47°E, 30.68°N). The observations were from October 1st, 2015 to October 31st, 2016. The height of the tower is 70 m and it was equipped with anemometers at four (4) different levels (i.e. 10 m, 30 m, 50 m and 70 m), and a 3D ultrasonic anemometer was mounted on the second level (i.e. 30 m above the ground surface). Table 1 shows the details of wind observation instruments.

The 3D ultrasonic anemometer is a Gill Instrument WindMaster Pro

Table 1
Details of wind observation instruments.

Instrument	Height (m)	Altitude (m)	Longitude	Latitude	Observation layers (m)
Tower	70	28	114.47°E	30.68°N	10/30/50/70
3D Ultrasonic anemometer	/	28	114.47°E	30.68°N	30

unit, which provides improved results of turbulence, energy balance and flux gradient. Ultrasonic anemometers have the advantages of stable operation since they cannot be damaged easily by wind. In this study, the 3D ultrasonic anemometer is used at a 10-Hz sampling frequency and permits 3D instantaneous wind speed data acquisition. Fig. 1 shows the wind tower and where the anemometer is placed, while Table 2 shows the technical indicators and parameters of the anemometer. Table 2 also exhibits the source website of such anemometer in the first line.

Fig. 2 shows the location of tower (114.47°E, 30.68°N), Wuhan national basic meteorological station (114.05°E, 30.60°N, refer to as Wuhan station in the following content) and Qingshan Ganghua aerosol observation station (114.39°E, 30.62°N, refer to as Qingshan Ganghua station in the following content). The observation tower is located on the side of the Yangtze River with small friction coefficient (Fig. 2a) and surrounded by open ground as shown in Fig. 2 (b ~ e). It is worth noting that the wind tower and Qingshan Ganghua station are located near the Yangtze River, both belong to the same climate of the Jiangnan Plain. The variabilities of PM_{2.5} concentration measured by aerosol stations in Wuhan are almost same (Huang et al., 2015). Qingshan Ganghua station is located near the industrial zone and is about 12 km away from the wind tower. It is the nearest one of all the aerosol observation stations to the wind tower, so it has the strongest representativeness.

This study also used reanalysis data contains geopotential height, wind field and PBLH, weather conditions data and boundary layer meteorology conditions data. The details of each data are exhibited in Table 3.

2.2. L-band radar data

The data of GFE(L) secondary wind measurement radar and GTS1 digital radiosonde of Wuhan station, referred to as L-band radar radiosonde data, covering period from 2015 to 2016. This dataset provides profiles of temperature, pressure, relative humidity and wind at the vertical resolution of 10 m with different heights from 0 to 2 km, which are recorded twice per day at 0700 LST and 1900 LST (Tang et al., 2018). Studies by Guo et al. (2016, 2019) used sounding data of boundary layer analysing at 0800 LST due to that a decoupled planetary boundary layer structure frequently occurred in the morning. Since the boundary layer structure often remains stable in the morning, this study used only 0700 LST radar data.

The temperature inversion layer is estimated by observing the part of the temperature profile that increases with the height. Such positive trend of temperature by the height increasing is conducive for pollutant accumulation.

2.3. Data quality control for 3D wind observation

Before the calculation of average wind temperature and turbulence parameters, the data were screened. The data on the pulsating winds in the bridge area were obtained and the data quality was determined. To ensure the quality of the observed data, the variance test method was applied to examine the outliers of the ultrasonic wind of the original data for the wind in three directions during the observation periods (Wang and Cao, 1994; Guo and Bian, 2007; Swain et al., 2008). The judgement was based on the following nomenclature: $|x_i - x| \geq n \cdot \sigma_x$. Where x_i is the observed value; x is the 30-min averaged value; σ_x is the standard deviation of the sample; and the value of n is 4. The variance test result indicates that the proportion of reliable data measured during the wind periods was greater than 99.9%.

2.4. Calculation of turbulence parameters

In this study, the vector analysis method was used to calculate the turbulence parameters. First, the main wind direction over a certain time interval was determined. Vector decomposition was then used to

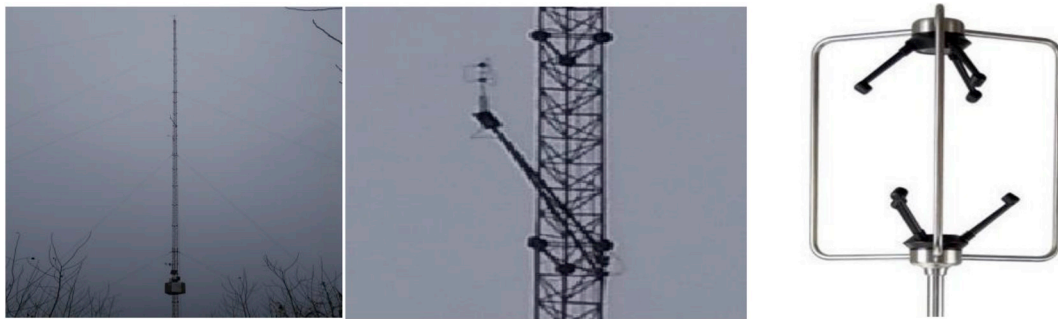


Fig. 1. Picture of the tower and 3D ultrasonic anemometer.

decompose the horizontal wind speed into the longitudinal wind speed along the main wind direction and the lateral wind speed perpendicular to the main wind direction (Kato et al., 1992; Xu and Sheng, 2001).

The three-dimensional wind speeds $u(t)$, $v(t)$, and $w(t)$ in the x , y and z directions measured by the ultrasonic anemometer are three real-value sequences. The horizontal average wind speed U and the wind direction angle Φ (angle between $u(t)$ and $v(t)$) were calculated using equations (2.1) and (2.2) at the time interval of 1 min:

$$U = \sqrt{u(t)^2 + v(t)^2} \tag{2.1}$$

$$\Phi = \arctg(v(t) / u(t)) \tag{2.2}$$

The vertical direction is the same as the instrument coordinate z -axis, so the vertical velocity is:

$$W = \overline{w(t)} \tag{2.3}$$

The coordinates of the instrument were rotated to the ϕ corner so that the instrument measures u consistent with the main wind direction. The obtained coordinate axes x , y and z represent the dominant winds $u(t)$, the crosswind $v(t)$ and the vertical wind direction $w(t)$, respectively. The projection $u'(t)$ and $v'(t)$ of the x and y -axes, respectively, represent the pulsating wind speeds of the longitudinal (main) wind and the horizontal (lateral) wind. They are calculated using equations (2.4) and (2.5) (Pang et al., 2006; Xu and Sheng, 2001):

$$u'(t) = u(t)\cos \Phi + v(t)\sin\Phi - U \tag{2.4}$$

$$v'(t) = -u(t)\sin \Phi + v(t)\cos \Phi \tag{2.5}$$

The vertical pulsating wind speed $w'(t)$ is given by equation (2.6):

Table 2
Technical indicators and parameters of the anemometer.

Source Website	(1) http://gillinstruments.com/products/anemometer/windmaster-pro.html#3axisanemometer (2) http://www.js1959.com/products_detail.aspx?pid=38&cateid=6		
Ultrasound sampling rate	32 Hz	Communication	RS232, 422, 485 Networking up to 26 anemometers
Measurement parameters	UVW, Polar, NMEA	Baud rate	2400–115,200
Average Wind speed measurement range, Resolution, Accuracy	0–3600 s 0–65 m/s, 0.01 m/s, 1.5% RMS	Sound speed measurement range, Resolution, Accuracy	300–370 m/s, 0.01 m/s, < ± 0.5% @ 20 °C
Wind direction measurement range, Resolution, Accuracy	(0–12 m/s) 0–359°, 0.1°, ±2° when <12 m/s	Size/Weight	750 mm*240 mm/1.7 kg
		Protection level	IP 65
		Operating temperature	–40–70 °C
		Operating humidity	5%–100%

$$w'(t) = w(t) - W \tag{2.6}$$

The projection $u'(t)$, $v'(t)$, and $w'(t)$ are the basic turbulent data time series used in statistical analyses of turbulence.

The turbulent intensity (TI) is the ratio of the standard deviation of the pulsation value to the average wind speed, equation (2.7). It is used to describe the degree of change in the wind speed with time and space and to measure the relative strength of wind speed pulsations. TI is an important feature in describing the characteristics of motion of atmospheric turbulence.

$$TI_i = \sigma_i / U \tag{2.7}$$

Here, $i = u, v, w$; σ_i represents the standard deviation of the pulsation velocities u' , v' , w' in the u, v, w directions; and U is the average wind speed in the main direction during the sub-sampling period of 3 s.

The turbulent kinetic energy (TKE) is an important variable in micro-meteorology and is a measure of the amount of turbulent energy present, which is directly related to the transport of momentum, heat and water vapor within the boundary layer. The relative importance of these physical processes determines the ability of a fluid to maintain turbulence or develop into turbulence; thus, it reflects flow stability. TKE was calculated based on equation (2.8) (Gorlé et al., 2009):

$$TKE(t) = \frac{1}{2} \left[u'(t)^2 + v'(t)^2 + w'(t)^2 \right] \tag{2.8}$$

The term momentum flux (F_m) refers to the amount of momentum transmitted per unit area per unit time. To calculate the momentum flux, this study used equation (2.9) following the method used in Pond et al. (2010) and Zielinski et al. (2018):

$$F_m(t) = \overline{u'(t)w'(t)} \tag{2.9}$$

Based on previous studies, the time interval is specified to be 30 min (Wang et al., 2010; 2011). Note that, where they are not specified, height and altitude values are given in ‘m’; wind speeds are given in ‘m/s’; wind directions are given in ‘°’; pulsating wind speeds are given in ‘m/s’; the turbulent intensity is dimensionless; the turbulent kinetic energy is given in ‘m²/s²’; and the momentum fluxes are given in ‘m²/s²’.

2.5. Calculation of the boundary layer structure index (BLSI)

The $BLSI$, which can effectively describe the atmospheric boundary layer structure, was accordingly developed and used to analyze the near-surface air quality.

$$BLSI = \frac{\bar{V}}{L \cdot \bar{\rho}} \frac{E_w}{VI} \tag{2.10}$$

where \bar{V} is the average wind speed at the ground and H m (unit is m/s), $\bar{\rho}$ represents the average density of the atmosphere at the ground and H

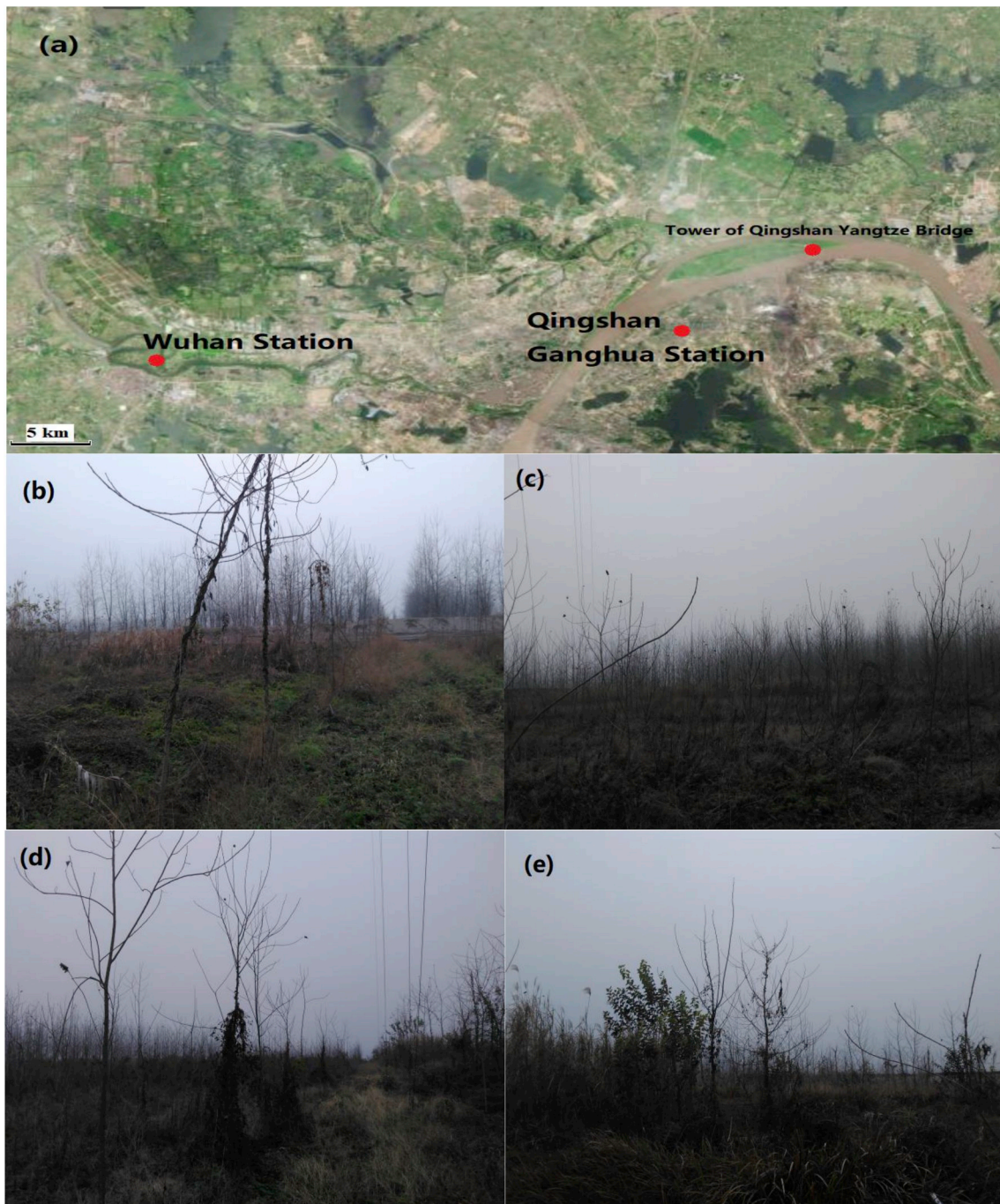


Fig. 2. (a) Location of bridge tower (114.47°E, 30.68°N, red dot in the right-hand-side), Wuhan station (114.05°E, 30.60°N, red dot in the left-hand-side) and Qingshan Ganghua station (114.39°E, 30.62°N, middle red dot); Topography and geomorphology around wind tower (b) North (c) East (d) South (e) West. (For interpretation of the references to color in this figure legend, the reader is referred to the Web version of this article.)

m (unit is kg/m^3), L denotes the condensation latent heat value of water vapor ($L = 2500.6 \text{ J/g}$), E_w represents the stable energy from the ground to the height H (unit is J/cm), VI is the ventilation index (unit is m^2/s), and $\frac{\bar{V}}{L \cdot \bar{p}}$ is used to ensure that the BLSI has no units. Details of the algorithm for the above parameters can be found in Zheng et al. (2019). In this study, we used H equal to 250 m.

2.6. Calculation of circulation patterns

Base on the studies by Jenkinson and Collison (1977), Lamb (2010) and Chen et al. (2016), we use Lamb-Jenkinson method to classify the

surface circulation patterns around Wuhan area (Fig. 3).

Based on sea level pressure of 16 selected points in Fig. 7 circulation indices are concluded as follows:

$$u = \frac{1}{2} [p[12] + p[13] - p[4] - p[5]] \tag{2.11}$$

$$v = \frac{1}{4} \frac{1}{\cos \alpha} [p(5) + 2p(9) + p(13) - p(4) - 2p(8) - p(12)] \tag{2.12}$$

$$V = \sqrt{u^2 + v^2} \tag{2.13}$$

Table 3

The details of data which have been used in this article.

Data type	Data content	Data source
Reanalysis data	Geopotential height at 850 hPa	NOAA: NCEP/NCAR Reanalysis
	Wind field at 850 hPa	ECMWF: ERA Interim, Daily
	Boundary layer height	
Meteorology conditions	Relative humidity	Wuhan station, Hubei Meteorological Bureau
	Visibility	
Aerosol observations	PM _{2.5} mass concentration	Qingshan Ganghua station, Wuhan Environmental Protection Bureau (WEPB)
3D wind speed	Wind speed per second in 3 directions	Hubei Meteorological Bureau
Boundary layer conditions	Profile of wind speed, wind direction, relative humidity, and air temperature	Wuhan station, Wuhan Meteorological Bureau

$$\xi_u = -\frac{\partial u}{\partial y} = \frac{1}{2} \frac{\sin \alpha}{\sin \alpha_1} [p(15) + p(16) - p(8) - p(9)] - \frac{1}{2} \frac{\sin \alpha}{\sin \alpha_2} [p(8) + p(9) - p(1) - p(2)] \quad (2.14)$$

$$\xi_v = \frac{\partial v}{\partial x} = \frac{1}{4} \frac{1}{2 \cos^2 \alpha} [p(6) + 2p(10) + p(14) - p(5) - 2p(9) - p(13) + p(3) + 2p(7) + p(11) - p(4) - 2p(8) - p(12)] \quad (2.15)$$

$$\xi = \xi_u + \xi_v \quad (2.16)$$

$$\begin{cases} v < 0, \alpha_g = \arctan(u/v) \\ v > 0, \alpha_g = \arctan(u/v) + 180^\circ \end{cases} \quad (2.17)$$

Note that, $p(n)$ ($n = 1, 2 \dots 16$) represents *slp* on each grid and α , α_1 and α_2 equal to 30, 25 and 35, respectively (Jones et al., 1993). V is geostrophic wind, while u and v are zonal and meridional component of V , respectively. ξ_u and ξ_v are meridional and zonal gradient of u and v , respectively, with the unit of hPa/10°. α_g represents the geostrophic wind direction.

Table 4 is the Lamb-Jenkinson circulation types. For instance, an area gets the circulation pattern as Anticyclone (A) which means such area is under control of Anticyclone. Furthermore, C represents Cyclone; N represents Northerly (Geostrophic wind); AN represents Anticyclone-Northerly.

2.7. Calculation of 3D planetary waves

Atmospheric signals are transmitted in stratosphere through wave-

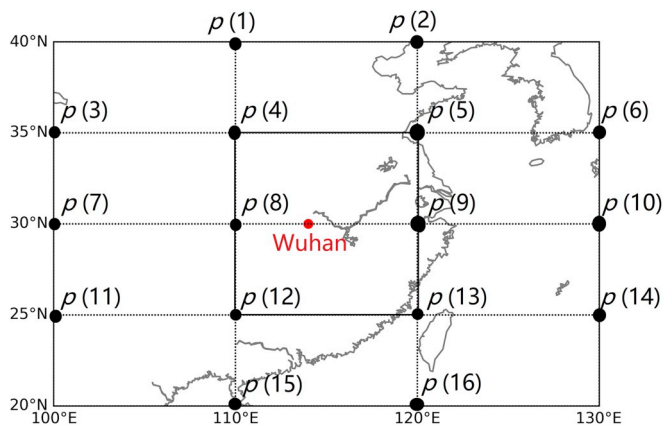


Fig. 3. The 16 grid points used to central difference in the selected area (black rectangle represents the chosen region for calculation the zonal and meridional components of geostrophic wind).

Table 4

Lamb-Jenkinson circulation types (Note: N, E, S, W represent the 4 directions of geostrophic wind, respectively).

$ \xi < V$ Horizontal flow	$ \xi \geq 2V$ Rotate	$V < \xi < 2V$ Mixed	$V < 6$ and $ \xi < 6$ Undefined
N (Northerly); NE E (Easterly); SE S (Southerly); SW W (Westerly); NW	$\xi \geq 2V$ C (Cyclone) $\xi \leq -2V$ A (Anticyclone)	$V \leq \xi < 2V$ CN; CNE; CE; CSE CS; CSW; CW; CNW $-2V < \xi \leq -V$ AN; ANE; AE; ASE AS; ASW; AW; ANW	U (Undefined)

current interaction. Eliassen-Palm flux (E-P flux) is introduced for the convenience of later investigation based on previous study by Trenberth (1986) and <http://www.ncl.ucar.edu/Applications/EPflux.shtml> Base on such studies, a wave action vector describing the propagation of 3D planetary waves is used to diagnose the cause of circulation anomalies. Such equation (Eq. (2.18)) is derived by Plumb (1985) and further used in the research by Tan et al. (2010).

$$F_s = p_0 \cos \phi \times \left(\begin{array}{c} v'^2 - \frac{1}{2\Omega a \sin 2\phi} \frac{\partial(v' \Phi')}{\partial \lambda} \\ -u'v' + \frac{1}{2\Omega a \sin 2\phi} \frac{\partial(u' \Phi')}{\partial \lambda} \\ \frac{2\Omega \sin \phi}{S} \left[v'T' - \frac{1}{2\Omega a \sin 2\phi} \frac{\partial(T' \Phi')}{\partial \lambda} \right] \end{array} \right) \quad \text{where } S = \frac{\partial \hat{T}}{\partial z} + \frac{\kappa \hat{T}}{H} \quad (2.18)$$

u' , v' , T' represent the eddy components of zonal wind, meridional wind and temperature minus the meridional mean, respectively. $p_0 = p/1000$; S represents static stability; \hat{T} represents regional average temperature, $z = -H \ln p$, H represents constant scale height. $\kappa = R/c_p$, in this manuscript, $\kappa = 0.286$. Φ is the longitude.

3. Results and discussion

3.1. Selection of typical fog-haze pollution days

Based on data provided by the Wuhan Environmental Protection Bureau (WEPB) and China Weather Network, Fig. 4 shows the (a) daily AQI and daily aerosol mass concentration (AMC) at 0700 LST and (b, c and d) turbulence parameters at 0700 LST from 1 December 2015 to 29 February 2016. Fig. 3a shows four (4) relatively high pollution periods (RHP1 to RHP4, shaded gray) when the AQI in each HP was greater than 150 (air quality level, AQL 4), indicating that the days in each HP were at least 'moderately polluted'. Fig. 3 shows that the turbulence activity was obviously weaker during the pollution periods than during the clean periods (RCP1 to RCP5, not shaded), especially the turbulence kinetic energy and turbulence flux. The correlation coefficient between AQI and TKE was -0.21 (at a 95% confidence interval), which meant TKE always remained at a lower level during pollution periods.

From these four (4) pollution periods, we selected seven (7) days that recorded 'heavy pollution', an AQI of more than 200 and no heavy rainfall or thunderstorm (such weather may harm the 3D ultrasonic anemometer and may have a negative influence on the observation results). The dates of the seven (7) severe fog-haze days were the 10th, 11th and 30th of December 2015; 17th and 18th of January 2016; and 8th and 24th of February 2016, corresponding to fog-haze days H1 to H7, respectively.

According to the national ambient air quality standard (AQs), grade II, a day that records a daily average concentration of PM_{2.5} of more than 75 $\mu\text{g}/\text{m}^3$ is regarded as a day with polluted air (GB3095).

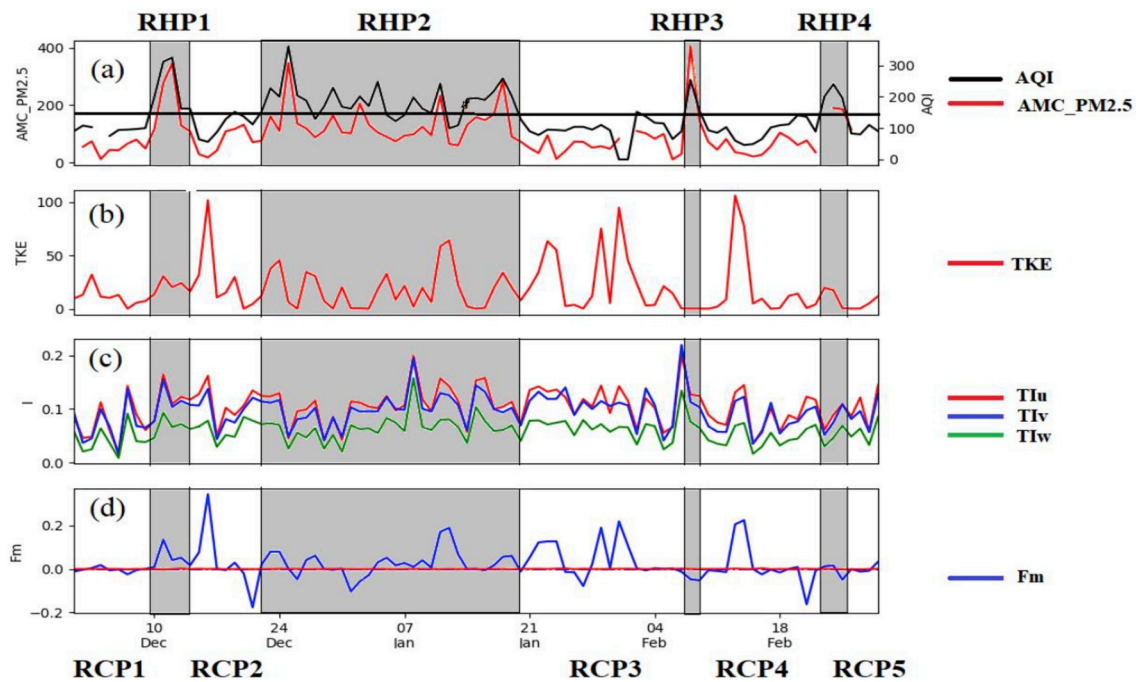


Fig. 4. Time series of (a) daily AQI and daily AMC at 0700 LST; turbulence parameters: (b) Turbulence kinetic energy (c) Turbulence intensity (d) Momentum flux at 0700 LST from December 1st, 2015 to February 29th, 2016 (Shaded: High-pollutant periods from HP1 to HP4).

3.2. Analysis of boundary layer and near-surface layer

The conditions of the atmosphere are usually stable from nightfall to early morning, and turbulence exchange is weak during this period. A previous study by Högström (1988) eliminated data obtained from 3D ultrasonic anemometers with frictional speeds $u^* < 0.1$ m/s. In this study, we calculated the friction velocities on fog-haze pollution days and found that friction velocities of less than 0.1 m/s make up a small fraction of the data. This result indicates that the atmospheric turbulence was strong in these chosen cases.

Based on data of atmospheric visibility (VISIB) and relative humidity (RH) provided by the Hubei Meteorological Bureau and aerosol mass concentration (AMC) data and according to a study by Wu (2008), heavy fog met two conditions of ‘RH > 90%’ and ‘VISIB < 1 km’, while heavy fog-haze met three conditions of ‘VISIB < 2 km’, ‘RH < 90%’ and ‘AMC_{PM2.5} > 75 µg/m³’. Table 5 shows the conditions of the selected fog-haze and heavy pollution episodes.

The selected processes in Table 5 are called ‘heavy pollution processes’ (P1 to P8). The following content will analyze the turbulence parameters for three (3) different periods before the pollution, during the pollution and after the pollution of each fog-haze day, respectively. A total of eight (8) heavy-pollution processes are discussed in the following section.

3.2.1. Boundary layer structure in fog-haze events

This subsection used L-band radar data provided by the Wuhan Meteorological Bureau to determine weather conditions and their variations in the boundary layer. Four boundary-layer features (solid-thin: wind direction ($D \times 30^\circ$); blue: wind velocity (U m/s); red: temperature (T °C); and green: relative humidity ($RH \times 10\%$)) were obtained from L-band radar observations (Fig. 5). Consistent with the conclusions of our previous studies (Mbululo et al., 2017, 2018), the inversion layer is vital for pollutant accumulation. Fig. 5a shows the existence of a weak inversion near-surface layer (below 100 m height) before a high-pollution event (HPE), but during the HPE, it becomes stronger and thicker (Fig. 5b). The thickness of the ground inversion layer was approximately 300 m, and another weak suspended inversion layer appeared at 1500 m. Moreover, the percentage of RH near the ground

was higher than that of other heights before and during the HPE, but it decreased obviously with height during the HPE. This high RH was favorable for pollutant accumulation, while a lower RH facilitated pollutant diffusion.

As for the wind direction (D), it behaved differently before and during the HPE. D had almost no change below 1500 m before the HPE, but it showed an obvious change during the HPE, especially below 900 m. These changes in D could be the catalyst for the formation of vertical turbulence intensities (TI_w). During the HPE, D changed significantly within a small range of heights (Fig. 5b), in contrast to what was observed before the HPE (Fig. 5a). Fig. 5c shows that the inversion layer became thinner than before. The dominant wind direction before, during and after fog-haze pollution events was a northerly wind. Normally, northerly winds bring significant amounts of air pollutants to Wuhan

Table 5 Selected fog-haze pollution days and heavy pollution episodes.

Pollution Day	Time Series	RH (%)	AMC _{PM2.5} (ug/m ³)	VISIB (m)	Number
H1 (9–11 Dec 2015)	18:00 (09th)~ 09:00 (10th)	>90%	>75	<300	P1
H2 (10–12 Dec 2015)	00:00 (12th)~ 11:00 (12th)	<90%	>320	<200	P2
H3 (29–31 Dec 2015)	19:00 (29th)~ 10:00 (30th) & 20:00 (30th)~ 09:00 (31st)	>90% & >93%	>105 & >105	<200 & <160	P3 & P4
H4 (16–18 Jan 2016) & H5 (17–19 Jan 2016)	19:00 (17th)~ 12:00 (18th)	>85%	>270	<2000	P5
H6 (7–9 Feb 2016)	00:00–08:00 (8th)	>95%	>140	<2000	P6
H7 (23–25 Feb 2016)	21:00 (23rd)~ 10:00 (24th) & 00:00–09:00 (25th)	63% & >95%	>100 & >140	<2000	P7 & P8

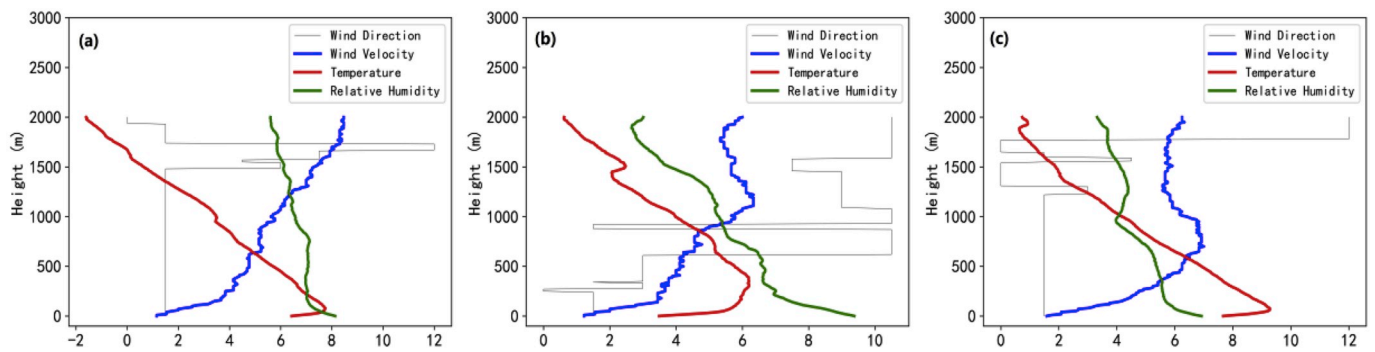


Fig. 5. Vertical profiles of averaged boundary-layer features (Solid-thin: Wind direction ($\times 30^\circ$); Blue: Wind velocity (m/s); Red: Temperature ($^\circ\text{C}$); Green: Relative humidity ($\times 10\%$) (a) before (b), during (c) and after fog-haze pollution events. Note that the boundary layer features before P2 and P7 were not similar to the others, as shown in Fig. 6. There was only a thin inversion layer from the ground to 40 m before P7, and the RH was low and was approximately the same amount at heights below 1500 m. The wind speed was also small, which facilitated pollutant accumulation. (For interpretation of the references to color in this figure legend, the reader is referred to the Web version of this article.)

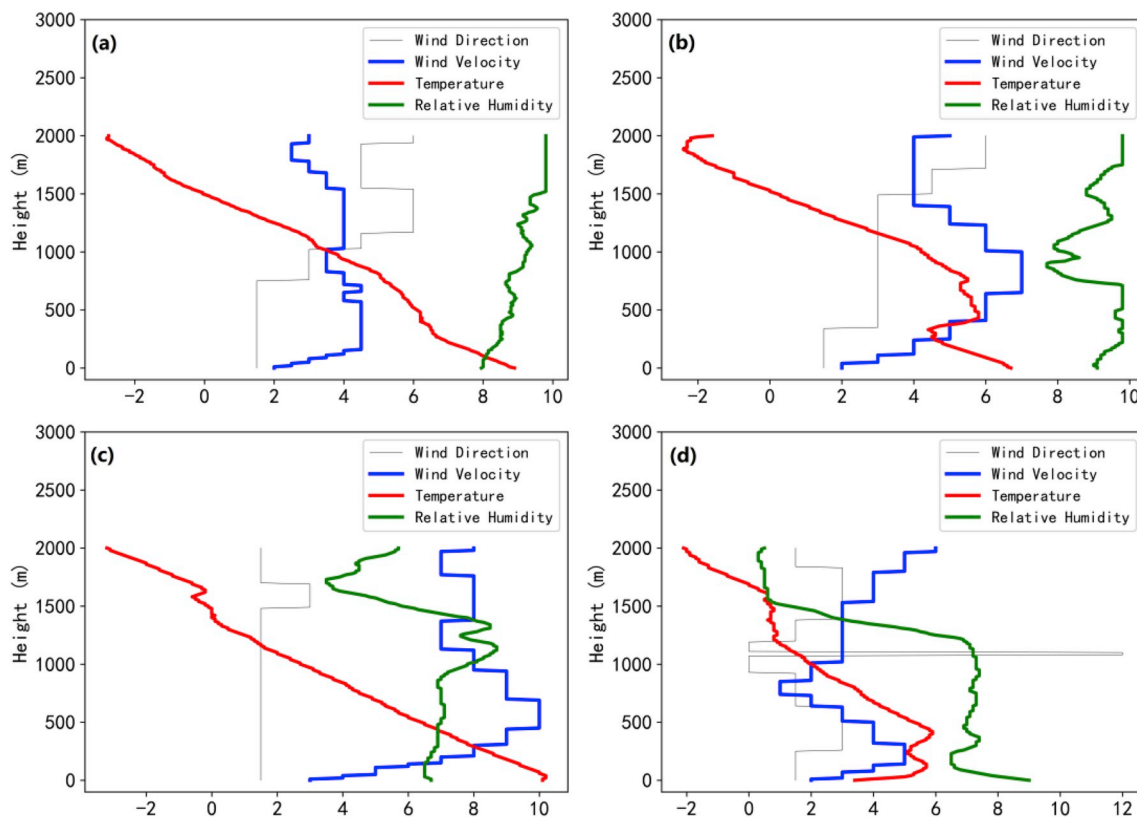


Fig. 6. Boundary-layer features before (a, c) and during (b, d) fog-haze pollution events in P2 (a, b) and P7 (c, d).

city as a result of transboundary movement.

During P2, an inversion layer appeared between altitudes of 300 m and 400 m, while during P7, there were two inversion layers: one was from 300 m to 400 m in height, and the second was from the ground to 100 m. This might be the result of weak ground inversion before P7.

We also used the boundary layer structure index (*BLSI*) to determine the correlation between the boundary layer and turbulence (based on a study by Zheng et al. (2019)). *BLSI* was calculated based on profiles of wind, temperature and relative humidity. Thermodynamic and dynamic effects were both considered in the calculation process. The *BLSI* was calculated by using L-band radar data at 0700 LST. The turbulence parameters for calculation of the correlation with *BLSI* were also selected at 0700 LST.

Table 6 shows the correlation coefficient among *BLSI*, *PBLH* and

turbulence parameters (including *TI*, *TKE*, and *F_m*) from the 1st of December 2015 to the 29th of February 2016. The results show that there was a significant negative correlation among the turbulence parameters, *PBLH* and *BLSI* (with the corresponding 95% confidence intervals). The size of *BLSI* determined the ability of the BL to diffuse pollutants; that is, the larger (smaller) *BLSI* is, the weaker (stronger) the diffusion ability of the BL. It was obvious that the larger (smaller) *BLSI* is, the lower (higher) *PBLH*, the weaker (stronger) *TI*, the weaker (stronger) the wind shear, the weaker (stronger) *TKE* and *F_m*, and the easier (more difficult) for the pollutant to accumulate. The above conclusions are partly consistent with the results from Guo et al. (2019) that higher *PBLH* values are due to climatologically stronger near-surface winds and higher solar heating and surface temperature, which are beneficial for the diffusion of air pollutants.

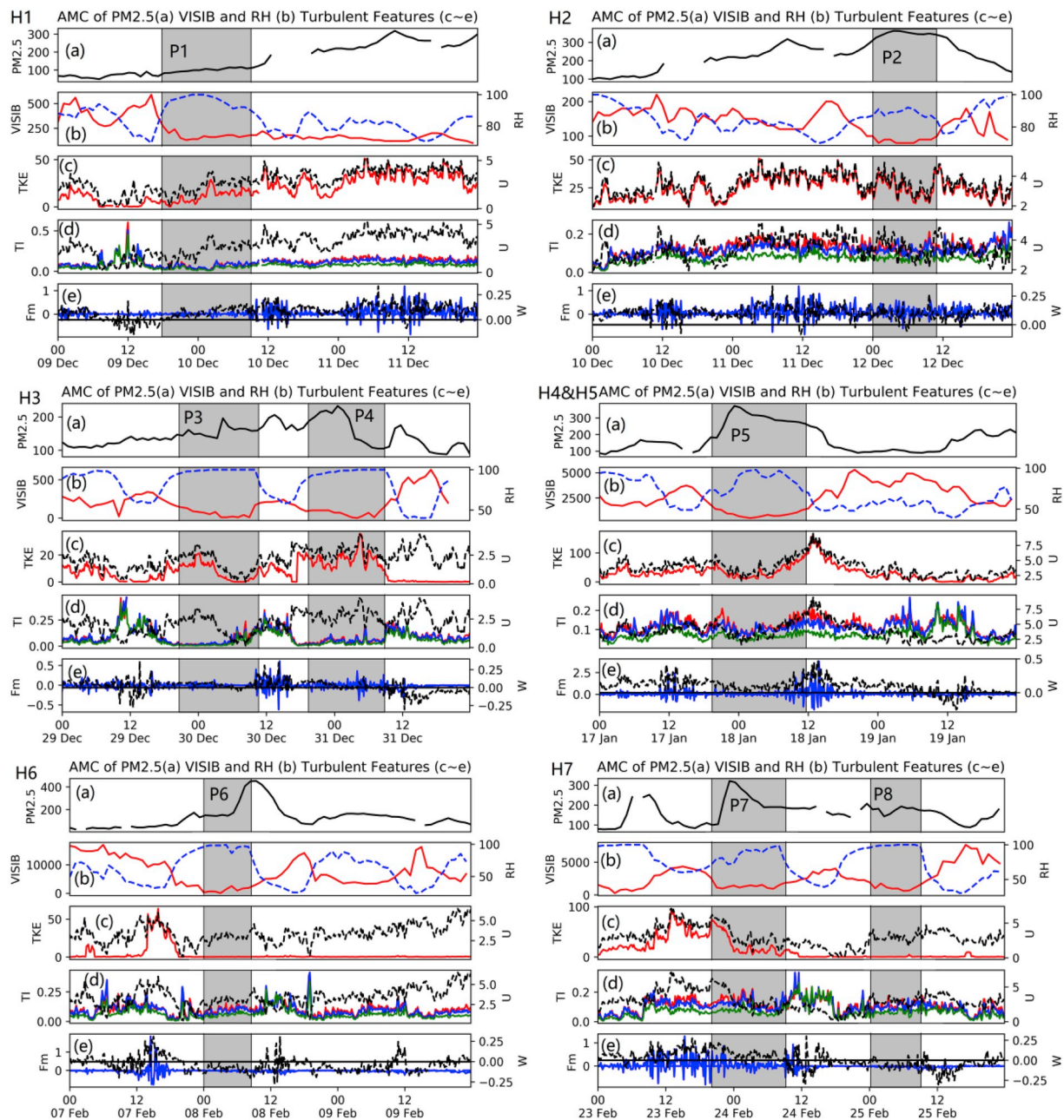


Fig. 7. Time series of weather and turbulence parameters during fog-haze days from H1 to H7, where the pollution episodes are marked by black frames. Each diagram contains 6 subfigures; the top one presents concentrations of $PM_{2.5}$, and the second one presents air visibility (red line) and relative humidity (blue dotted line). The black dotted line represents the vertical velocity in the fifth figure, and the same dots represent the horizontal velocity in the remaining figures (c to e). From the third figure to the fifth figure, the colored lines represent turbulence kinetic energy, turbulence intensities (red: TI_u ; blue: TI_v ; and green: TI_w) and momentum flux. (For interpretation of the references to color in this figure legend, the reader is referred to the Web version of this article.)

Table 6

Correlation coefficients between $BLSI$ and turbulence parameters (Note: The sample size is 79 after removing the missing values, and the correlation coefficients reach statistically significant for $p \leq 0.05$).

	TI_u	TI_v	TI_w	TKE	F_m	PBLH
PBLH	0.29	0.22	0.18	0.69	0.62	–
BLSI	–0.22	–0.25	–0.23	–0.27	–0.28	–0.43

3.2.2. Turbulence parameters of fog-haze pollution days

As shown in Fig. 7, the vertical velocity maintains upward flow during most days. During these days, the horizontal wind speed was frequently below 5 m/s and rarely exceeded 5 m/s. These conditions with high RH and low VISIB represent the fog-haze pollution process.

Note that the turbulence parameters include TI_i ($i = u, v, w$), TKE, and F_m . First, TI_i featured the amounts of wind pulsating in three (3) directions. The values of TI_i during the breeze process were often larger than those during the gale process, except for H2, where TI_i often stays stable throughout the whole period. In H2, RH was below 90% during the pollution episode but reached 100% before and after the onset of heavy pollution. This is probably because water vapor is highly related

Table 7

Abnormal turbulence characteristics and their lead times (unit: min) prior to heavy pollution processes.

		P1	P2	P3	P4	P5	P6	P7	P8
TI_u	Abnormal values	0.604	Lower RH	0.460	0.344	0.197	0.232	Lower RH	0.271
	Lead times	360	F_m , TKE are active	540	500	460	230	F_m , TKE are active	750
TI_v	Abnormal values	0.508		0.465	0.320	0.206	0.293		0.332
	Lead times	360		480	500	460	230		750
TI_w	Abnormal values	0.455		0.411	0.273	0.129	0.164		0.266
	Lead times	360		540	500	430	230		750
TKE	Abnormal values	0		0	0	0	0		0
	Lead times	660		610	900	500	270		740
F_m	Abnormal values	0		0	0	0	0		0
	Lead times	80		180	230	130	360		390

to turbulence. TKE always decreased to near zero before the onset of heavy pollution and always increased rapidly and then remained in a high state before the decrease in AMC . F_m also behaved similar to TKE when AMC was low and decreased to near zero before the onset of heavy pollution. It is thought that F_m maintained a high state to transport momentum to the upper level of the atmosphere by positive vertical velocity and strong turbulence kinetic energy.

Based on the descriptions given in Table 5, it can be concluded that P1 to P4 form one group with the lowest $VISIB$, while P5 to P8 form another group with higher $VISIB$ but with relatively lower RH . The pollution processes of P2 and P7 are not similar to those of other fog-haze pollution events, as both are lower- RH pollution processes. The time series of the turbulence factors are shown in Fig. 7 (including H1 to H7 with no shading and P1 to P8 with gray shading).

Our previous study (Qin et al., 2018) analyzed a heavy fog-haze pollution event in Hunan Province and found that the turbulence intensity reached an anomalous peak value when the turbulence kinetic energy and turbulent flux decreased to zero (0) and it was less than 130 min prior to the onset of heavy pollution. Moreover, a study by Zhang et al. (2010) found that turbulent fluxes had abnormal disturbances nearly 360 min prior to the formation of heavy fog.

Notably, atmospheric turbulence presents abnormal characteristics (abnormal for TI : reach peak values 2 times larger than average; abnormal for TKE and F_m : decrease to a very low state near zero) before heavy pollution processes. Compared with the wind speed, the representation of turbulence is more meaningful. Note that fog-haze pollution accounted for a large proportion of pollution periods in P2 and P7, while TKE and F_m showed significant changes before P2 and P7, but their values did not reach zero. Table 7 lists the lead times of abnormal turbulence characteristics prior to pollution processes.

3.3. Circulation pattern and boundary layer

First, to analyze the circulation pattern, the reanalysis data from NCEP/NCAR for seven (7) different typical fog-haze days (H1 to H7) were used in this study. A study by Chen et al. (2016) revealed that pollution events frequently appear in wintertime in Wuhan city. There are a total of six (6) kinds of circulation patterns (A; C; E; AE; NE; and SE) during pollution processes in Wuhan city. Normally, A, E and AE occur in wintertime. This conclusion is based on the Lamb-Jenkinson method (Jenkinson and Collison, 1977; Lamb, 2010).

Table 8 shows the circulation patterns of heavy pollutant events from H1 to H7 (including P1 to P8), and Table 9 shows the geostrophic wind gradients. It can be recognized that patterns A and NE account for the first and second proportions of the whole patterns, respectively. This means that when weather pollution in Wuhan is severe, it is generally under the control of an anticyclone, especially before severe fog-haze periods. That is, such rotation circulation patterns are conducive to the accumulation of pollutants.

Tables 8 and 9 and Fig. 7 show that the $PM_{2.5}$ concentration in P1 and P2 increases until the end of P2. In addition, turbulence activity becomes active after P2. This also shows that A-type and NE-type circulations are

beneficial to pollutant accumulation, while SE-type circulations, which are less common, may be beneficial to stimulate turbulence activity and lead to pollutant diffusion. P3 and P4 are nearly controlled by A-type circulation, and the concentration of $PM_{2.5}$ increases obviously during the two processes. The main circulation pattern in the first and middle stages of P5 is NE type, in the early stage of P5 is ANE type, and at the end stage is ASE type. The overall situation is similar to that of P1 and P2. The duration of P6 is short, and the circulation pattern is A in the first and middle stages and SW at the end. The turbulence energy is still weak. A combined analysis of P7 and P8 shows that the whole process occurs under A-type circulation. The $PM_{2.5}$ concentration increases obviously in P7 and is stable in P8 and later. Turbulence activity decreases to a minimum of nearly zero during P7, which is one of the reasons why the $PM_{2.5}$ concentration does not change significantly in P8. We also chose 2 periods on clean days (C1 and C2, where the weather was good for observation without any rainfall or snowfall) for comparison and found that an A-type circulation pattern was maintained throughout the whole clean periods. However, the geostrophic wind gradients of C1 and C2 are relatively smaller than those of severe fog-haze periods from P1 to P8. Table 8 shows the geostrophic wind gradients based on the above table. The geostrophic wind gradient values of P1 and P5 are larger due to the existence of N-type circulation, while those of A-type circulation in other processes are smaller.

3.4. Analysis of typical fog-haze event

According to historical weather data provided by the China Weather Network, the weather in H6 was mainly sunny (in the following content, E6 represents 08 February 2016 from H6). The predominant wind direction of E6 was southerly wind, which indicated that under the influence of this wind direction, pollutants from local emissions played a leading role since the transboundary movement was relatively weak. This section is based on E6 to analyze the turbulence characteristics during the stabilization stage, the growth stage and the dissipation stage of $AMC_{PM_{2.5}}$. As shown in Fig. 8, the variation in $AMC_{PM_{2.5}}$ is separated into three (3) stages: the stabilization stage was from 0100 LST to 0500 LST, the growth stage was from 0500 LST to 0900 LST, and the dissipation stage was from 0900 LST to 1300 LST for E6.

In the stabilization stage, the turbulence was weak, and water vapor was abundant in the near-surface layer. The stability of the atmosphere was not conducive to diffusion of pollutants. Note that at this stage, the city was in the middle of the night with less anthropogenic emissions. In the growth stage, the vertical wind speed started to increase after 0700 LST, and the horizontal wind speed started to increase after 0800 LST. Normally, the sun began to rise in winter at approximately 0700 LST, and as a result, the solar radiation was strengthened. The solar radiation changed the structure of the boundary layer by increasing the air temperature. The changes in the stability of atmospheric stratification resulted in enhancement of the turbulence and evaporation of water vapor; therefore, these changes were expected to increase the diffusion of pollutants. Nevertheless, $AMC_{PM_{2.5}}$ significantly increased in this stage, which might be the result of human activities. It is thought that a

Table 8
Circulation patterns of severe fog-haze periods from P1 to P8 and C1 and C2.

Severe Periods	P1	P2	P3	P4	P5	P6	P7	P8	Clean Days Period 1 (C1)	C2
Before	1400 LST 9 Dec 2015	AE	2000 LST 11 Dec 2015	A	1400 LST 29 Dec 2015	A	1400 LST 30 Dec 2015	A	2000 LST 15 Dec 2015	A
During	2000 LST	NE	0200 LST 12 Dec 2015	A	2000 LST	A	2000 LST	A	0200 LST 16 Dec 2015	A
	0200 LST 10 Dec 2015	NE	0800 LST	ASE	0200 LST 30 Dec 2015	A	0200 LST 31 Dec 2015	A	0800 LST	A
After	0800 LST	NE			0800 LST	A			1400 LST	A
	1400 LST	ANE	1400 LST	ASE	1400 LST	A	0800 LST	A	2000 LST	A
	P5		P6		P7		P8		Clean Days Period 2 (C2)	
Before	1400 LST 17 Jan 2016	NE	2000 LST 7 Feb 2016	A	2000 LST 23 Feb 2016	A	2000 LST 24 Feb 2016	A	1400 LST 14 Feb 2016	A
During	2000 LST	ANE	0200 LST 8 Feb 2016	A	0200 LST 24 Feb 2016	A	0200 LST 25 Feb 2016	A	2000 LST	A
	0200 LST 18 Jan 2016	NE	0800 LST	A	0800 LST	A	0800 LST	A	0200 LST 15 Feb 2016	A
After	0800 LST	NE			0800 LST	A			0800 LST	A
	1400 LST	ASE	1400 LST	SW	1400 LST	A	1400 LST	A	1400 LST	A

Table 9
Geostrophic wind gradients of severe fog-haze periods from P1 to P8 and C1 and C2.

Severe Fog-Haze Periods	P1	P2	P3	P4	P5	P6	P7	P8	C1	C2
Before	-5.71	-18.90	-20.74	-15.10	-4.35	-13.55	-28.99	-23.01	-27.60	-29.61
During	-1.64	-18.77	-17.27	-15.26	-10.79	-16.21	-24.99	-18.95	-27.97	-39.95
	7.14	-12.15	-15.67	-15.65	-6.52	-12.82	-25.77	-17.47	-28.84	-32.87
	6.48		-13.44		0.94				-32.82	-30.42
After	-8.96	-13.29	-15.10	-18.72	-13.62	-7.18	-23.05	-14.55	-32.86	-30.30

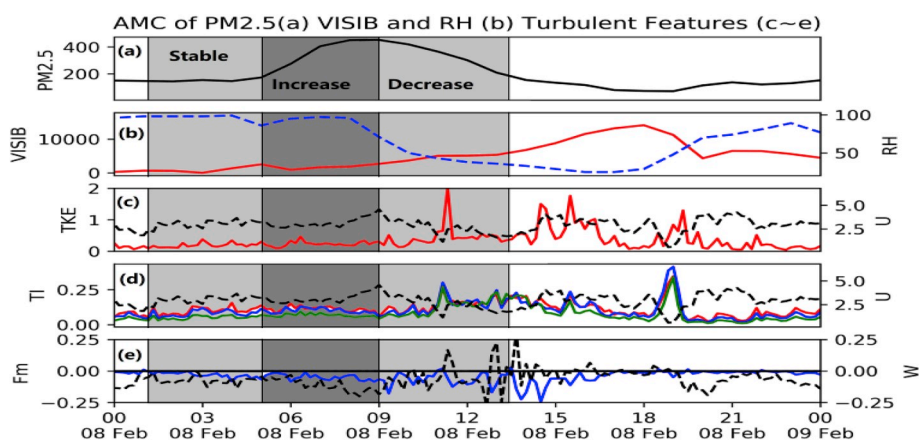


Fig. 8. Time series of weather and turbulence parameters from 0000 LST to 2350 LST on 08 February 2016 (during H6) (the structure of Fig. 8 is the same as that of Fig. 7).

high concentration of aerosols scattered the solar radiation and delayed the weakening of stable stratification, which resulted in the accumulation of pollutants. The turbulence in the dissipation stage was stronger than that in the first two stages, especially TKE and F_m . The stable stratification was finally destroyed, resulting in enhancement of the turbulence diffusion capacity and the evaporation of water vapor.

The average RH and turbulence parameters in the three (3) stages in E6 are summarized in Table 10. Stable atmospheric stratification and weak turbulence activity were the preconditions of pollutant accumulation, and abnormal turbulence characteristics occurred prior to heavy pollution. The change in the stable structure of the boundary layer caused by solar radiation was a precondition of pollutant diffusion. The

Table 10
Averaged RH and turbulence parameters of three stages in E6.

	RH	Tl_u	Tl_v	Tl_w	TKE	F_m
Steady	97.5	0.097	0.079	0.051	0.189	-0.028
Increase	94.25	0.115	0.102	0.068	0.237	-0.049
Decrease	65.0	0.134	0.130	0.115	0.446	-0.067

accumulation of pollutants usually occurred in the early morning, the existence of a high concentration of aerosols resulted in a more stable boundary layer structure, and the time of weakening of the stable stratification was delayed. When the stable stratification condition disappeared, the turbulence activity began to increase, and AMC began to decrease. The values of F_m were negative, indicating that momentum transfer increases from the stabilization period to the dissipation period.

Gao et al. (2015) simulated the January boundary layer characteristics during fog-haze pollution in the North China Plain. Their results showed that AMC reached its maximum at night. The feedback mechanism mainly occurred at approximately 1000 LST and 1600 LST during the daytime, which made the atmospheric stratification more stable and facilitated the accumulation of pollutants, thus promoting the formation of fog. In this study, there was a significant negative correlation between the BLSI and the turbulence characteristics under this background. That is, the stronger that the BLSI was, the more stable the BL, the weaker the turbulence, and the weaker the diffusion ability of the atmosphere to pollutants. At 0700 LST in winter when the external pollution was weak, the pollutants accumulated due to stable stratification and scattering of solar radiation by aerosols. The ground temperature was reduced, and

the maintenance time of the static and stable boundary layer structure was prolonged by the pollutants, showing feedback.

To further analyze turbulence anomalies, the wind components at 850 hPa from NCEP/NCAR reanalysis data were used to analyze the

average three-dimensional planetary wave flux (F_3) of H6 and the wave flux anomalies at various times (each value is reduced by 100 times, which is convenient for mapping). Fig. 9 shows an obvious wave source area in the northeast of Wuhan, with the wave energy propagating

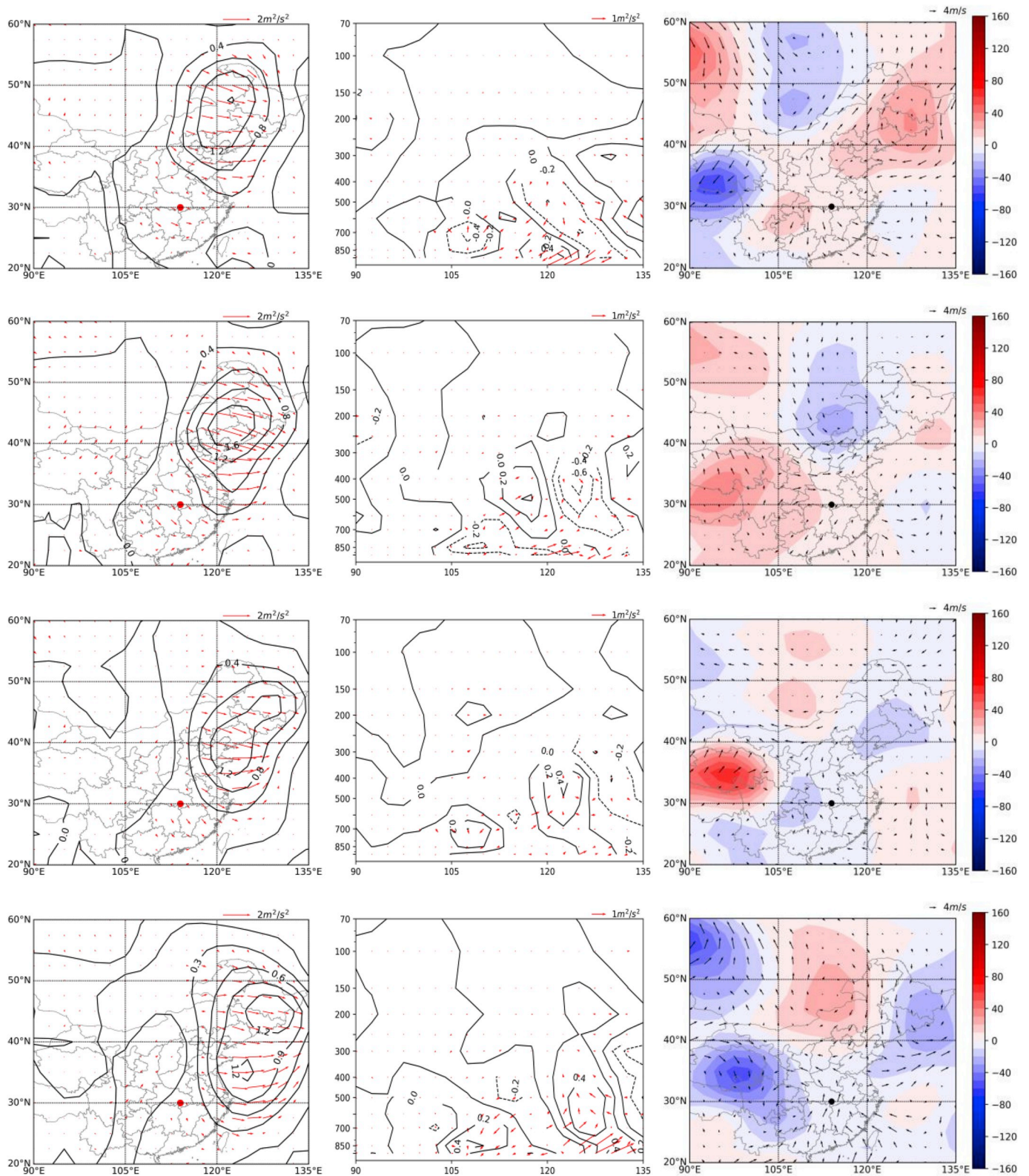


Fig. 9. F_3 anomaly values for four (4) stages (on the left and middle panels, from top to bottom, the middle panels present longitude-altitude sections at 30°N) in E6. The right panels present the geopotential and wind vectors at 850 hPa in E6 (the vector scale in the upper-right denotes a value of 4 m/s). (The date and time for the top panel to the bottom are 2000 LST on 7 Feb 2016 and 0200 LST, 0800 LST and 1400 LST on 8 February 2016, respectively).

upward and eastward. Approximately 4 h (240 min) before P6, i.e., near the time point when turbulence anomalies occurred, the location of the wave source and sink regions were further northwestward than that during P6 and after P6, and the horizontal wave energy transport over Wuhan was obviously stronger than that after P6. The vertical profile diagrams show that the wave energy propagating eastward from 110°E before P6 converges with the wave energy propagating westward from high altitude. The convergence area was approximately 850 hPa near 115°E over Wuhan.

The meridional component of F_s over Wuhan has an anomalous wave train path. The center of the positive anomaly moves eastward with time. The wave energy transmitted westward above 120°E weakens obviously with time. The direction of wave energy transmission over Wuhan changed from eastward before P6 to westward after P6. The right panels show that Wuhan is between two high pressures and show an A-type circulation pattern (saddle pattern). In combination with this A-type pattern, the weak wind field and the northerly wind around Wuhan were conducive to pollutant accumulation. With the passage of time, the saddle field gradually disappears, and the wave-flow interaction weakens the high pressure in northeastern Wuhan. After P6, the type of circulation pattern changes from A to SW.

4. Conclusion

Based on the above analysis, this study concludes the following:

- 1) Before and during heavy fog-haze pollution events, there were weak pressure and saddle circulation patterns. Inversion layers were generated before a heavy fog-haze pollution event and became thicker during the pollution process. The inversion layers generally occurred at an altitude of approximately 600 m. There was a significant negative correlation between $BLSI$ and $PBLH$, as well as turbulence parameters. Such that the larger the $BLSI$ was (the lower the $PBLH$ was), the weaker the turbulence and the easier for the pollutants to accumulate. A feedback mechanism existed between solar radiation and $AMC_{PM2.5}$ when $PM_{2.5}$ was about to diffuse. The wind speed was generally below 5 m/s and rarely exceeded this speed on the selected fog-haze days. The turbulence was active (weak) when AMC was low (high). The turbulence variation characteristics had special representations during such days, especially before and during pollution events.
- 2) Tl_i reached abnormal peak values when fog-haze pollution processes were about to happen and maintained a stable condition when RH was not high. In most cases, the value of Tl_i reached abnormally high values approximately 8 h prior to the heavy fog-haze pollution process. TKE and F_m both decreased to near zero before the heavy fog-haze pollution process. F_m often presented abnormal disturbances before heavy pollution, and the time at which such signals occurred prior to heavy pollution processes was often before that of TKE . Moreover, TKE and F_m often presented an active phase before and during lower- RH pollution processes, such as in P2 and P7.
- 3) With the passage of time, the planetary wave transmission over Wuhan changes obviously; the horizontal component decreases, with the wave source and sink regions move eastward; and the wave energy convergence over Wuhan gradually weakens. The wave-flow interaction weakens the high pressure in northeastern Wuhan, possibly indicating that the occurrence of turbulence anomalies may be related to the regulation of atmospheric circulation by wave-flow interaction.

Generally, abnormal turbulence characteristics appeared before the heavy fog-haze pollution processes throughout the above analysis, and this study tried to determine a detailed mechanism of how this happened. However, due to the lack of temperature observations at different heights, features of air stability and heat flux were not calculated. Therefore, the specific mechanism of turbulence anomalies needs

further study to be verified. If the relationship between large-scale circulation patterns and small-scale turbulence variation characteristics could be thoroughly analyzed, it would be possible to predict the concentration of pollutants, prevent and control pollution and guarantee the health and safety of people.

Acknowledgement

This work was supported by the National Key Research and Development Programme of China (2016YFA0602002). We would like to express our sincere thanks to the Hubei Provincial Meteorological Bureau for providing data and support for this study.

References

- Bergot, T., 2013. Small-scale structure of radiation fog: a large-eddy simulation study quarterly. *Q. J. Roy. Meteorol. Soc.* 139 (673), 1099–1112. <https://doi.org/10.1002/qj.2051>.
- Chen, L., Zhi, X., Qin, J., et al., 2016. Surface atmospheric circulation types of air pollution and its relationship with concentration of air pollutants in Wuhan. *Meteorol. Mon.* 42 (7), 819–826 (In Chinese).
- Creamean, J.M., Neiman, P.J., Coleman, T., et al., 2016. Colorado air quality impacted by long-range-transported aerosol: a set of case studies during the 2015 pacific northwest fires. *Atmos. Chem. Phys.* 16 (18), 12329–12345. <https://doi.org/10.5194/acp-16-12329-2016>.
- Guo, J., Li, Yuan, Cohen, J., et al., 2019. Shift in the temporal trend of boundary layer height in China using long-term (1979–2016) radiosonde Data. *Geophys. Res. Lett.* 46, 6080–6089. <https://doi.org/10.1029/2019GL082666>.
- Guo, J., Miao, Y., Zhang, Y., Liu, H., Li, Z., Zhang, W., et al., 2016. The climatology of planetary boundary layer height in China derived from radiosonde and reanalysis data. *Atmos. Chem. Phys.* 16 (20) <https://doi.org/10.5194/acp-16-13309-2016>, 13, 309–313, 319.
- Gao, Y., Zhang, M., Liu, Z., et al., 2015. Modeling the feedback between aerosol and meteorological variables in the atmospheric boundary layer during a severe fog-haze event over the north china plain. *Atmos. Chem. Phys.* 15 (8), 1093–1130. <https://doi.org/10.5194/acp-15-4279-2015>.
- Gorlé, C., Beeck, J., Rambaud, P., et al., 2009. Cfd modelling of small particle dispersion: the influence of the turbulence kinetic energy in the atmospheric boundary layer. *Atmos. Environ.* 43 (3), 673–681. <https://doi.org/10.1016/j.atmosenv.2008.09.060>.
- Guo, J., Bian, L., 2007. Measured CO₂ concentration and flux at 16 m height during corn growing period on the north China plain. *Chin. J. Atmos. Sci.* 31 (4), 695–707. <https://doi.org/10.1002/jrs.1570> (In Chinese).
- Han, S., Liu, J., Hao, T., et al., 2018. Boundary layer structure and scavenging effect during a typical winter haze-fog episode in a core city of BTH region, China. *Atmos. Environ.* 179, 187–200. <https://doi.org/10.1016/j.atmosenv.2018.02.023>.
- Huang, Y., Liu, C., Zeng, K., et al., 2015. Spatio-temporal distribution of PM_{2.5} in Wuhan and its relationship with meteorological conditions, 2013–2014. *Ecol. Environ. Sci.* 24 (8), 1330–1335. <https://doi.org/10.16258/j.cnki.1674-5906.2015.08.011> (In Chinese).
- Högström, U., 1988. Non-dimensional wind and temperature profiles in the atmospheric surface layer: are-evaluation. *Bound-Lay. Meteorol.* 42 (1), 55–78. <https://doi.org/10.1007/BF00119875>.
- Jones, P.D., Hulme, M., Briffa, K.R., 1993. A comparison of lamb circulation types with an objective classification scheme. *Int. J. Climatol.* 13 (6), 655–663. <https://doi.org/10.1002/joc.3370130606>.
- Jenkinson, A.F., Collison, F.P., 1977. An initial climatology of gales over the North Sea. In: *Synoptic Climatology Branch Memorandum. Meteorological Office, Bracknell. No 62*.
- Kato, N., Ohkuma, T., Kim, J.R., et al., 1992. Full scale measurements of wind velocity in two urban areas using an ultrasonic anemometer. *J. Wind Eng. Ind. Aerod.* 41 (1–3), 67–78. [https://doi.org/10.1016/0167-6105\(92\)90394-P](https://doi.org/10.1016/0167-6105(92)90394-P).
- Li, Z., Guo, J., Ding, A., et al., 2017. Aerosol and boundary-layer interactions and impact on air quality. *Natl. Sci. Rev.* 4, 810–833. <https://doi.org/10.1093/nsr/nwx117>.
- Lamb, H.H., 2010. Types and spells of weather around the year in the british isles: annual trends, seasonal structure of the year, singularities. *Quart. J. Roy. Meteor. Soc.* 76 (330), 393–429. <https://doi.org/10.1002/qj.49707633005>.
- Mbululo, Y., Qin, J., Hong, J., et al., 2018. Characteristics of atmospheric boundary layer structure during PM_{2.5} and ozone pollution events in Wuhan, China. *Atmos. Basel* 9 (9). <https://doi.org/10.3390/atmos9090359>.
- Mbululo, Y., Qin, J., Yuan, Z., 2017. Evolution of atmospheric boundary layer structure and its relationship with air quality in Wuhan, China. *Arab. J. Geosci.* 10 (22) <https://doi.org/10.1007/s12517-017-3257-9>.
- Miao, Y., Liu, S., Zheng, Y., et al., 2016. Modeling the feedback between aerosol and boundary layer processes: a case study in Beijing, China. *Environ. Sci. Pollut. Res.* 23 (4), 3342–3357. <https://doi.org/10.1007/s11356-015-5562-8>.
- Petäjä, T., Järvi, L., V K, et al., 2016. Enhanced air pollution via aerosol-boundary layer feedback in China. *Sci. Rep.* <https://doi.org/10.1038/srep18998>.
- Philipp, A., Beck, C., Huth, R., et al., 2016. Development and comparison of circulation type classifications using the COST 733 dataset and software. *Int. J. Climatol.* 36 (7), 2673–2691. <https://doi.org/10.1002/joc.3920>.
- Pasch, A., Macdonald, C., Gilliam, R., et al., 2011. Meteorological characteristics associated with PM 2.5 air pollution in cleveland, Ohio, during the 2009–2010

- cleveland multiple air pollutants study. *Atmos. Environ.* 45 (39), 7026–7035. <https://doi.org/10.1016/j.atmosenv.2011.09.065>.
- Pond, S., Phelps, G., Paquin, J., et al., 2010. Measurements of the turbulent fluxes of momentum, moisture and sensible heat over the ocean. *Asia-Pac. J. Atmos. Sci.* 28 (6), 901–917. [https://doi.org/10.1175/1520-0469\(1971\)028<0901.MOTTFO>2.0.CO;2](https://doi.org/10.1175/1520-0469(1971)028<0901.MOTTFO>2.0.CO;2).
- Pang, J., Song, L., Lin, Z., et al., 2006. Comparison and application of two methods for analysing the turbulence characteristics of wind. *J. Tongji Univ. Nat. Sci.* 34 (1), 27–32. <https://doi.org/10.3321/j.issn:0253-374X.2006.01.006> (In Chinese).
- Plumb, R., 1985. On the three-dimensional propagation of stationary waves. *J. Atmos. Sci.* 42 (3), 217–229. [https://doi.org/10.1175/1520-0469\(1985\)042<0217:OTTDPO>2.0.CO;2](https://doi.org/10.1175/1520-0469(1985)042<0217:OTTDPO>2.0.CO;2).
- Qin, J., Yuan, Z., Zeng, X., et al., 2018. Analysis on the characteristics of physical quantities variation in near surface layer during the severe haze process in Yueyang. *Clim. Environ. Res.* 23 (5), 533–542. <https://doi.org/10.3878/j.issn.1006-9585.2017.17050> (In Chinese).
- Ren, Y., Zheng, S., Wei, W., et al., 2018. Characteristics of turbulent transfer during episodes of heavy haze pollution in Beijing in winter 2016/17. *J. Meteorol. Res. Proc.* 32 (1), 69–80. <https://doi.org/10.1007/s13351-018-7072-3>.
- Shen, L., Mickley, L., 2017b. Effects of el niño on summertime ozone air quality in the eastern United States. *Geophys. Res. Lett.* 44 (24), 12543–12550. <https://doi.org/10.1002/2017GL076150>.
- Shen, L., Mickley, L., 2017a. Seasonal prediction of US summertime ozone using statistical analysis of large-scale climate patterns. *Proc. Natl. Acad. Sci. U.S.A.* <https://doi.org/10.1073/pnas.1610708114>.
- Swain, D., Wark, T., Bishop, G., 2008. Using high fix GPS data to determine the relationships between fix rate, prediction errors and patch selection. *Ecol. Model.* 212 (3–4), 273–279. <https://doi.org/10.1016/j.ecolmodel.2007.10.027>.
- Tang, Z., Chen, L., Qin, J., Zheng, X., 2018. Numerical simulation of the local flow field and the boundary layer structure in the pollution process in Wuhan. *Resour. Environ. Yangtze Basin* 27 (11), 2540–2547. <https://doi.org/10.11870/cjlyzyhj201811015> (In Chinese).
- Tan, G., Chen, H., Sun, Z., Den, W., 2010. Linkage of the cold event in January 2008 over China to the north atlantic oscillation and stratospheric circulation anomalies. *Chin. J. Atmos. Sci.* 34 (1), 175–183 (In Chinese).
- Trenberth, K.E., 1986. An assessment of the impact of transient eddies on the zonal flow during a blocking episode using localized Eliassen-Palm flux diagnostics. *J. Atmos. Sci.* 43 (19), 2070–2087. [https://doi.org/10.1175/1520-0469\(1986\)0432.0.CO;2](https://doi.org/10.1175/1520-0469(1986)0432.0.CO;2).
- Wei, W., Zhang, H., Wu, B., et al., 2018. Intermittent turbulence contributes to vertical diffusion of PM_{2.5} in the North China Plain. *Atmos. Chem. Phys.* <https://doi.org/10.5194/acp-2018-121>.
- Wang, Y., Xu, X., Liu, H., et al., 2016. Analysis of land surface parameters and turbulence characteristics over the Tibetan plateau and surrounding region. *J. Geophys. Res. Atmos.* 121 (16), 9540–9560. <https://doi.org/10.1002/2016JD025401>.
- Wang, J., Wang, S., Jiang, J., et al., 2013. Impact of aerosol–meteorology interactions on fine particle pollution during China’s severe haze episode in January 2013. *Environ. Res. Lett.* <https://doi.org/10.1088/1748-9326/9/9/094002>.
- Wang, L., Qin, J., Chen, Z., et al., 2010. Study on the abnormal characteristics of physical quantity fields at the near-surface layer for two rainstorm processes in Huangshi of eastern Hubei. *Meteorol. Mon.* 36 (12), 28–34. <https://doi.org/10.3788/HPLPB20102207.1462> (In Chinese).
- Wang, L., Qin, J., Chen, Z., 2011. A case study on the characteristics of the physical quantity fields on the near-surface layer during a snowstorm process. *Trans. Atmos. Sci.* 34 (3), 305–311. <https://doi.org/10.1016/B978-0-444-53599-3.10005-8>.
- Wu, D., 2008. Discussion the distinction between haze and fog and analysis and processing of data. *Environ. Chem.* 27 (3), 327–330 (In Chinese).
- Wang, C., Cao, W., 1994. Spectral characteristics of surface-layer turbulence over the suburbs of Tianjin. *J. Meteorol. Res. Proc.* 52 (4), 484–492.
- Wilcox, E., Thomas, R., Praveen, P., et al., 2016. Black carbon solar absorption suppresses turbulence in the atmospheric boundary layer. *Proc. Natl. Acad. Sci. U.S.A.* 113 (42), 11794–11799. <https://doi.org/10.1073/pnas.1525746113>.
- Xu, Y., Sheng, Z., 2001. Field measurements of di Wang tower during typhoon York. *J. Wind Eng. Ind. Aerod.* 89 (1), 73–93. [https://doi.org/10.1016/S0167-6105\(00\)00029-5](https://doi.org/10.1016/S0167-6105(00)00029-5).
- Zheng, X., Qin, J., Liang, S., Yuan, Z., et al., 2019. The development of boundary layer structure index (BLSI) and its relationship with ground air quality. *Atmosphere* 10 (1), 3. <https://doi.org/10.3390/atmos10010003>.
- Zieliński, M., Fortuniak, K., Pawlak, W., et al., 2018. Long-term turbulent sensible-heat-flux measurements with a large-aperture scintillometer in the centre lodz, Central Poland. *Bound-layer. Meteorol.* <https://doi.org/10.1007/s10546-017-0331-5>.
- Zhong, J., Zhang, X., Dong, Y., et al., 2017. Feedback effects of boundary-layer meteorological factors on explosive growth of PM_{2.5} during winter heavy pollution episodes in Beijing from 2013 to 2016. *Atmos. Chem. Phys.* <https://doi.org/10.5194/acp-2017-845>.
- Zhang, H., Liu, X., Zhu, H., et al., 2010. Characteristics of turbulent transfer during the strong wind period in the northern suburbs of Beijing. *Chin. J. Atmos. Sci.* 34 (3), 661–668. <https://doi.org/10.3724/SP.J.1037.2010.00186> (In Chinese).